First-principles study of the excitonic effect on two-photon absorption of semiconductors: Theory and application to MoS$_2$ and WS$_2$ monolayers

You-Zhao Lan[*] and Xiao-Hu Bao

Institute of Physical Chemistry, Key Laboratory of the Ministry of Education for Advanced Catalysis Materials,
College of Chemistry and Life Sciences, Zhejiang Normal University, Zhejiang, Jinhua 321004, China

Based on the Bethe-Salpeter equation eigenstates, we present a first-principles many-body formalism for calculating the two-photon absorption (TPA) coefficient of semiconductors. We apply this formalism to calculate the TPA spectra of MoS$_2$ and WS$_2$ monolayers. The all-electron full-potential linearized augmented plane wave based functions are used for solving the Bethe-Salpeter equation. The calculated TPA spectra exhibit significant excitonic effects when compared to those based on the independent particle approximation. The physical origin of TPA excitonic transitions of MoS$_2$ and WS$_2$ monolayers are revealed by tracing the sum-over-states process. We show that the spin-orbit coupling effect leads to characteristic double peaks with an interval of half spin-orbit splitting energy. These double peaks mainly originate from the transitions at the vicinity of K point. We compare our calculated two-photon absorption spectra to experimental and other theoretical results.

I. INTRODUCTION

It has been well known that the excitonic effect must be considered to accurately understand the one-photon absorption (OPA) spectrum of materials [1–9]. The excitonic effect includes the electron-hole interaction on the calculated absorption spectrum, which goes beyond the independent particle approximation (IPA). As reported by Rohlfing and Louie [8], with inclusion of the excitonic effect, the calculated OPA spectrum is in excellent agreement with the experimental one in terms of peak positions and line shape. For nonlinear optical properties, such as second- and third-harmonic generations, the excitonic effect is also important [10–12] and significantly modifies these nonlinear optical properties [13–15]. For example, a giant enhancement of the second-harmonic emission has been observed for WSe$_2$ monolayer [15]. The excitonic effect significantly modifies the intensity of peaks and the shape of spectrum for the third-harmonic generation [13]. We also notice that the inclusion of excitonic effects is necessary for understanding the two-photon absorption (TPA) spectrum of materials [16–19]. The TPA spectroscopy is an important tool to study the excited state of system. The TPA and OPA spectra generally provide the complementary information for the excited state of system because they have different selection rules. For instance, for a centrosymmetric system, one- and two-photon allowed transitions are mutually exclusive, and thus the TPA spectrum can provide the dark states that do not appear in the OPA spectrum. Similar to OPA, many simple or empirical models based on a few bands within IPA have been developed to understand the TPA of solids [20,21]. Obviously, information provided by these models is limited for the excited state of system because these models miss

the possible excitonic state of system. Recently, Berkelbach *et al.* [17] have provided a formalism, combining a fully k-dependent few-orbital band structure with a many-body Bethe-Salpeter equation (BSE) treatment, to calculate the one and two-photon absorption spectra using the generalized Fermi golden rule. Although they used a model dielectric function and neglected the spin-orbit coupling effect for simplicity, the feature of bright and dark singlet excitons of monolayer transition-metal dichalcogenides has been well understood.

In our present paper, based on the fully *ab-initio* BSE eigenstates, we present a first-principles many-body formalism to calculate the TPA spectrum. We consider a random phase approximation dielectric function with local field contributions and the spin-orbit coupling effect. The strategy is first to solve the self-consistent Kohn–Sham equations with the generalized gradient approximation (GGA) of the Perdew–Burke–Ernzerhof (PBE) functional [22] combined with the all-electron full-potential linearized augmented-plane wave (FP-LAPW) method [23], and then to solve the BSE to obtain the excited states of system, finally based on the BSE eigenstates, we use the time-dependent perturbation theory to obtain an expression for calculating the TPA coefficient. Applications are performed on two monolayer transition-metal dichalcogenides, i.e., MoS$_2$ and WS$_2$, whose OPA spectra including the excitonic effect have been well studied [4,5,24,25]. Compared to the IPA-TPA spectra, the BSE-TPA ones exhibit significant excitonic effects. For WS$_2$ monolayer, the BSE-TPA spectrum is partially consistent with the experimental TPA ones. Meanwhile, we also calculate the BSE-OPA spectra of MoS$_2$ and WS$_2$ monolayers, which are in excellent agreement with the very recent experimental results [6] in terms of peak positions and line shape. By tracing the sum-over-states (SOS) process of the TPA coefficients, we discuss the physical origin of the TPA states.

*lyzhao@zjnu.cn

In Sec. II, we describe a theoretical strategy for calculating the TPA spectrum. In Sec. III, we give the computational details, after which the physical origin of TPA of MoS_2 and WS_2 monolayers is discussed and a comparison between the theoretical and experimental TPA spectra for WS_2 monolayer is made. Finally, the conclusions are given in Sec. IV.

II. THEORY

We first sketch out how to obtain the optical transition rate by solving the following time-dependent Schrödinger equation in the *interaction* picture:

$$i\hbar \frac{\partial \psi(t)}{\partial t} = [H_0 + V(t)]\psi(t), \qquad (1)$$

where H_0 and $V(t)$ are the static unperturbed Hamiltonian and the time-dependent perturbation operator (describing the interaction between the light radiation and material), respectively. The $V(t)$ in the interaction picture is defined as

$$V(t) = e^{(i/\hbar)H_0 t} V_0 e^{-i\omega t + (\eta/\hbar)t} e^{-(i/\hbar)H_0 t}, \qquad (2)$$

where V_0 is a static operator, ω is an applied field frequency, and η is a positive infinitesimal energy. The various order transition rates for a direct optical transition from an initial state $|i\rangle$ to a final state $|f\rangle$ (two eigenstates of H_0), accompanied by the simultaneous absorption of n photons (each of frequency, ω), are given by the matrix elements of V_0 and the Dirac delta function as [21]

$$W_n(\omega) = \frac{2\pi}{\hbar} \left| \sum_{a_1, a_2, \cdots, a_{n-2}, a_{n-1}} \frac{\langle f|V_0|a_{n-1}\rangle \langle a_{n-1}|V_0|a_{n-2}\rangle}{[E_{n-1} - E_{n-2} - (n-1)\hbar\omega]} \cdots \frac{\langle a_2|V_0|a_1\rangle \langle a_1|V_0|i\rangle}{(E_2 - E_1 - 2\hbar\omega)(E_1 - E_i - \hbar\omega)} \right|^2 \delta(E_f - E_i - n\hbar\omega), \quad (3)$$

where $|a_1\rangle, |a_2\rangle, \ldots |a_{n-1}\rangle$ are all possible intermediate states, and the corresponding energies are $E_1, E_2, \ldots, E_{n-1}$, respectively. A detailed procedure for deriving the first, second, and third-order optical transition rates [i.e., $n = 1, 2, 3$ in Eq. (3)] can be found in the textbook [3].

Then, we consider two types of unperturbed Hamiltonians (H_0) to calculate the optical transition rate of a bulk system. One is one-particle Hamiltonian (H_0^{1p}) within the IPA, the other is effective two-particle Hamiltonian (H_0^{2p}) based on the BSE. Within the IPA, the eigenstate and corresponding energy in Eq. 3 are taken from the independent particle band structure, that is, $|i\rangle$ and $|f\rangle$ are assumed to be the occupied valence band (v) and the unoccupied conduction band (c), respectively, and E_f–E_i denotes the transition energy from a valence band (E_v) to a conduction band (E_c). At this time, the total first and second-order transition rates per unit volume for a bulk system can be written by

$$W_1^{(1)}(\omega) = \frac{4\pi}{\hbar} \frac{1}{\Omega} \sum_{c,v,k} |\langle c|V_0|v\rangle|^2 \delta(E_c - E_v - \hbar\omega), \qquad (4)$$

$$W_2^{(2)}(\omega) = \frac{4\pi}{\hbar} \frac{1}{\Omega} \sum_{c,v,k} \left| \sum_{a_1} \frac{\langle c|V_0|a_1\rangle \langle a_1|V_0|v\rangle}{E_1 - E_v - \hbar\omega} \right|^2 \times \delta(E_c - E_v - 2\hbar\omega), \qquad (5)$$

where a factor of 2 is included for electron-spin degeneracy, Ω is the volume of unit cell, and the k-dependences of eigenstates and their energies are compressed for clarity.

The use of effective two-particle Hamiltonian (H_0^{2p}) based on the BSE make the electron-hole interaction be included in the calculation of optical transition rates. The H_0^{2p} is defined as [7,26]

$$H_0^{2p} = H_0^{1p} + H^{eh}, \qquad (6)$$

where H_0^{1p} has the same form as one-particle Hamiltonian based on the IPA, and H^{eh} is the electron-hole interaction term which includes the direct attraction interaction term ($H^{eh,d}$) and the exchange term ($H^{eh,x}$). While the H_0^{1p} describes the independent-particle excitation, the H^{eh} means the coupling between different independent-particle transitions ($v \to c$). In

this case, the eigenstates of H_0^{2p} indicate the electron-hole excited states $|S\rangle$ (i.e., $H_0^{2p}|S\rangle = E^S|S\rangle$). The $|S\rangle$ is usually given by the linear combination of independent-particle excitations $|vck\rangle$ (i.e., $|vk\rangle$ to $|ck\rangle$) as

$$|S\rangle = \sum_{c,v,k} A_{c,v,k}^S |vck\rangle. \qquad (7)$$

Now, $W_T^{(1)}$ and $W_T^{(2)}$ are written by

$$W_1^{(1)}(\omega) = \frac{4\pi}{\hbar} \sum_{S_f} |\langle 0|V_0|S_f\rangle|^2 \delta(E_f^S - \hbar\omega), \qquad (8)$$

$$W_2^{(2)}(\omega) = \frac{4\pi}{\hbar} \sum_{S_f} \left| \sum_m \frac{\langle 0|V_0|S_m\rangle \langle S_m|V_0|S_f\rangle}{E_m^S - \hbar\omega} \right|^2 \delta(E_f^S - 2\hbar\omega), \qquad (9)$$

where $|0\rangle$ is the electronic ground state (initial state) and $|S_m\rangle$ and $|S_f\rangle$ are the intermediate and final states of an optical transition with the excitation energies of E_m^S and E_f^S, respectively.

For the interaction between light radiation and material, we use $V_0 = (e/mc)A \cdot p$ at the momentum gauge, where A is the vector potential associated with the applied light radiation and p is the momentum operator for the electron. In this case, Eqs. (4) and (5) require the computation of momentum matrix between independent-particle states (e.g., $\langle c|p|v\rangle$), and Eqs. (8) and (9) require $\langle 0|p|S_f\rangle$ and $\langle S_m|p|S_f\rangle$. As p is a one-particle operator, we can easily compute the $\langle 0|p|S_f\rangle$ and $\langle S_m|p|S_f\rangle$ in terms of the general rule for the matrix element of one-particle operator between Slater determinants [3,27] and the renormalization of momentum matrix elements of IPA [10,28,29], that is,

$$\langle 0|p|S_f\rangle = \sum_{c,v,k} \frac{E_f^S}{E_c^{IPA} - E_v^{IPA}} A_{c,v,k}^S p_{cv,k}^{IPA}, \qquad (10)$$

$$\langle S_m|p|S_f\rangle = \sum_{c_1,c_2,v_1,v_2,k} A_{c_1,v_1,k}^{S_m*} A_{c_2,v_2,k}^{S_f} \left(p_{c_1 c_2,k}^{IPA} \delta_{v_1 v_2} + p_{v_1 v_2,k}^{IPA} \delta_{c_1 c_2} \right). \qquad (11)$$
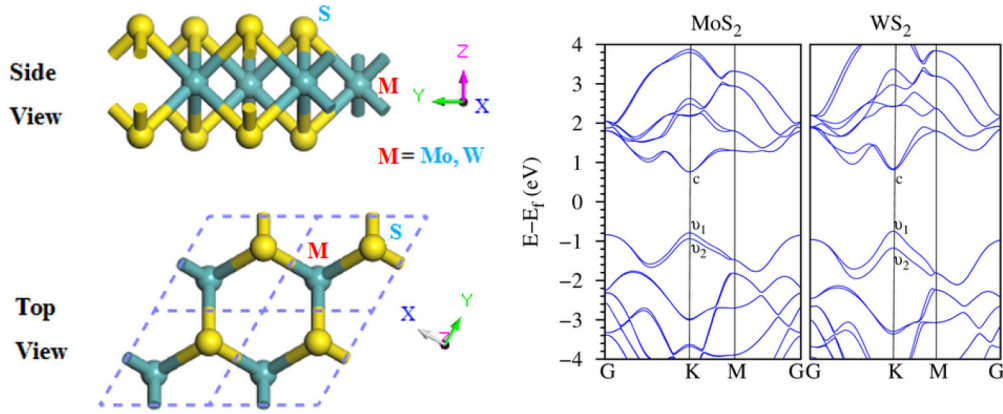
FIG. 1. Crystal structures (left) and band structures (right) of MoS_2 and WS_2 monolayers. The dash lines (left) denote the unit cell. The c indicates the degenerate c1 and c2 conduction bands.

Finally, the n-photon absorption coefficient α_n is related to W_n by

$$\alpha_n(\omega) = \frac{n\hbar\omega}{I^2} W_n(\omega), \qquad (12)$$

where I is the applied light radiation intensity, which is related to A_0 by $A^2_0 = 2\pi cI/(n\omega^2)$, where n is the refractive index and c is the speed of light in vacuum. Hereafter, we use the notation α and β for OPA and TPA coefficients, respectively.

III. APPLICATIONS

A. Computational method

Crystal structures of MoS_2 and WS_2 monolayers are shown in Fig. 1. The unit cell with D_{3h} symmetry was optimized by using the density functional theory within the GGA of PBE combined with the FP-LAPW method [23], as implemented in the ELK code [30]. A k-point mesh of $10 \times 10 \times 1$, force threshold of 2×10^{-4} a.u., and stress threshold of 1×10^{-5} a.u. were used for optimizations. The relaxation of the unit cell was included in optimizations. A vacuum spacing larger than 15 Å was used to ensure negligible interaction between the slabs. The optimized structures were used for the band structure calculations. We performed the band structure calculations by using the GGA-PBE combined with the all-electron FP-LAPW method [23], as implemented in ELK code [30]. A k-point mesh of $18 \times 18 \times 1$ was used for the band structure calculations. The spin-orbit coupling was considered. The optimized lattice parameters, electronic energy gaps, two transition energies at the K point, and the spin-orbit splitting energy are shown in Table I. The band structures and spin-orbit splitting energies are in good agreement with previous reports [5,31–33]. For instance, the MoS_2 monolayer is a direct gap semiconductor with an electronic energy gap (E_g) at the K point, where the conduction band minimum is doubly degenerate and the valence band maximum is split due to the spin-orbit coupling.

For the optical properties, the energy band structures within the IPA were obtained by solving the self-consistent Kohn–Sham equations with the GGA-PBE functional, and the excitation states including electron-hole interaction were obtained by solving the BSE with a basis linearly expanded by

the IPA states [Eq. (7)]. The spin-orbit coupling was included in all calculations. The corresponding momentum matrix elements were also calculated by a homemade ELK interface which reads p^{IPA} to calculate the BSE states based momentum matrix in terms of Eqs. (10) and (11). As the GGA-PBE calculation generally underestimates the band gap of solid, the scissor correction was used and the corresponding scissor value was given by the difference between the theoretical and experimental electronic energy gaps (Table I).

We calculated the TPA coefficients parallel to the monolayer plane ($\beta = \beta_{xx=yy}$, x, y directions defined in Fig. 1). We make a convergence test on the k-grid for the TPA calculation. Figure 2 shows the k-dependence of β of WS_2 monolayer with a scissor value of 0.82 eV calculated by (2.38–1.56) (Table I). Similar to the OPA calculation by Molina-Sánchez *et al.* [4], we cannot obtain a very good convergence (i.e., overlap of line shape). However, we observe a very similar distribution of absorption peaks for 18×18, 24×24, and 30×30 k grids (with the limit of computer resource, we can only calculate the k grids up to 30×30). A smaller 12×12 k grid leads to an absence of the first two-photon excitonic peak which appears in the experimental TPA spectrum [19]. Furthermore, as will be shown below, the OPA based on the 18×18 k grid has agreed well with a very recent experimental OPA [6] in terms of peak positions and binding energy of excitonic states, and also note that the 18×18 k grid yield the converged excitonic binding energy within 0.05 eV [4]. Thus we will further discuss the TPA spectrum based on the excited states obtained from the 18×18 k-grid BSE calculations.

B. Origin of TPA of MoS_2 and WS_2 monolayers

Now, we further discuss the TPA spectrum of WS_2 monolayer. We also discuss the TPA spectrum of MoS_2 monolayer whose OPA including excitonic effect has been well studied [4,5,24,25]. Based on the convergence test above, we also use the 18×18 k-grid and the scissor value ($E_g^{Exp} - E_g^{PBE}$) to calculate the TPA spectrum of MoS_2 monolayer. Note that the difference in experimental conditions, such as substrate and temperature, leads to different electronic energy gaps. For consistence, we used the experimental electronic energy gaps based on the

TABLE I. Optimized lattice parameters ($a = b$ in Å), electronic energy gaps (E_g^{PBE} in eV), two transition energies (E_{v1c} and E_{v2c} in eV) at the K point, and the spin-orbit splitting energies (Δ_{so} in eV) based on the PBE calculation. E_{sc} is the scissor correction value (eV) for the BSE calculation. The available experimental electronic energy gaps (E_g^{Exp} in eV) are included.

	$a = b$	E_g^{PBE}	E_g^{Exp}	E_{v1c}	E_{v2c}	Δ_{so}	E_{sc}
MoS$_2$	3.21	1.55	2.16 ± 0.04[a]	1.55	1.70	0.15	0.61
			2.15 or 2.35[b]				
WS$_2$	3.18	1.56	2.38 ± 0.06[a]	1.56	1.99	0.43	0.82
			2.47[c]				

[a]On fused quartz substrate with the STS measurement at room temperature [6,34].
[b]On highly ordered pyrolytic graphite substrate with the scanning tunneling spectroscopy (STS) measurement at 77 K [35].
[c]On monolayer graphene with the STS measurement at ∼5 K [36].

same experimental measurement [6,34] for MoS$_2$ and WS$_2$ monolayers (i.e., 2.16 and 2.38 eV in Table I). Figure 3 shows the TPA spectra of MoS$_2$ and WS$_2$ monolayers based on the BSE and IPA calculations. We also show in Fig. 3 the theoretical and experimental [6] OPA spectra to understand the TPA spectra. The experimental OPA spectra were obtained by Rigosi *et al.* [6] who used the optical reflectance contrast measurements at room temperature. They also reported the electronic band gap (Table I) based on the scanning tunneling spectroscopy measurements at room temperature. Note that we used this electronic band gap to make a scissor correction in the BSE calculations. As shown in Figs. 3(c) and 3(d), our theoretical OPA are in good agreement with the experimental ones in terms of peak positions. Note that we have made a rigid shift of 0.05 and 0.10 eV for MoS$_2$ and WS$_2$ monolayers, respectively. These rigid shifts are valid because the experimental electronic band gaps used in our BSE calculations have uncertainty (Table I). And also note that the rigid shift mainly leads to the rigid shift of peak position and hardly affect the intensity of peak [37,38]. As shown in Table II, various theoretical and experimental methods yield very close transition energies for A and B excitons. However, very different electronic band gaps are reported in these theoretical and experimental works, which leads to different excitonic binding energies in the range of 0.2–1.0 eV [4–6,9,19,24,31,35,39–41]. Our present theoretical results are

in good agreement with the theoretical [4] and experimental [6] ones.

While the OPA spectra show the light exciton, the TPA spectra help us to identify the dark exciton [18] because TPA has different selection rule from OPA [11,46]. To show the importance of excitonic effect in the TPA spectrum, we first consider the TPA spectrum based on the IPA calculation (IPA-TPA). As shown in Figs. 3(a) and 3(b), the IPA-TPA spectra exhibit two distinct peaks (labeled by Q_1 and Q_2) near the onset of spectrum. To obtain an insight into the origin of these two peaks, we trace the SOS process and show in Fig. 4 the distribution of contributions from the k points of the first Brillouin zone [$\sum_{vc}$ in Eq. (5)] used in the SOS calculation. We can see that the contributions mainly come from the k points near six vertices of the first Brillouin zone such as K and K′ points (see size of points). Furthermore, the energy difference between the Q_1 and Q_2 peaks is close to half the spin-orbit splitting energy. For instance, by tracing the SOS process, we find that Q_1 and Q_2 of MoS$_2$ monolayer can mainly attributed to the transition from v_1 to c and from v_2 to c (Fig. 1), respectively. At these k points near the K point (Fig. 1), the spin-orbit splitting energy is 0.136 eV which is about twice the energy difference between Q_1 and Q_2 peaks (0.06 eV in Table II). Thus the Q_1 and Q_2 peaks are associated with the spin-orbit coupling effect.

Then, we discuss the TPA spectra based on the BSE calculations (BSE-TPA). In Figs. 3(a) and 3(b), we show the TPA spectra with the input photon energy below the OPA edge. Near the OPA edge, the TPA spectra possibly exhibit a strong OPA resonance due to the denominator of ($E^s-\hbar\omega$) [Eq. (9)]. For instance, the OPA edge of MoS$_2$ monolayer is located at 1.91 eV (Table II), which leads to a strong resonant enhancement of β near 1.9 eV [Fig. 3(a)]. Hereafter, we focus on the input photon energy below the OPA edge to avoid the OPA resonance. As shown in Fig. 3, there are distinct TPA excitonic peak with the input photon energy below the OPA edge. The selected characteristic peaks are labeled by $P_{1,2,3,4}$ and the corresponding photon energies are given in Table II. Likewise, to obtain an insight into the origin of these peaks, we identify the corresponding two-photon excitonic state by tracing the SOS process and show in Fig. 4 the distribution of weight ($\sum_{vc}|A^S_{vck}|^2$ in Eq. (7) for the k points of the first Brillouin zone used to construct the excitonic state in Eq. (7). For the P_1 and P_2 peaks, similar to the Q_1 and Q_2 peaks, the contributions mainly come from the k points near six vertices of the first Brillouin zone. However, compared to
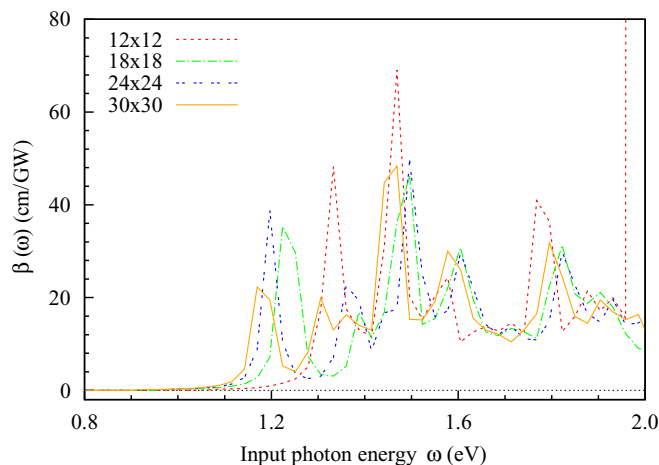
FIG. 2. The k dependence of the TPA spectra for WS$_2$ monolayer with a scissor value of 0.82 eV (Table I).
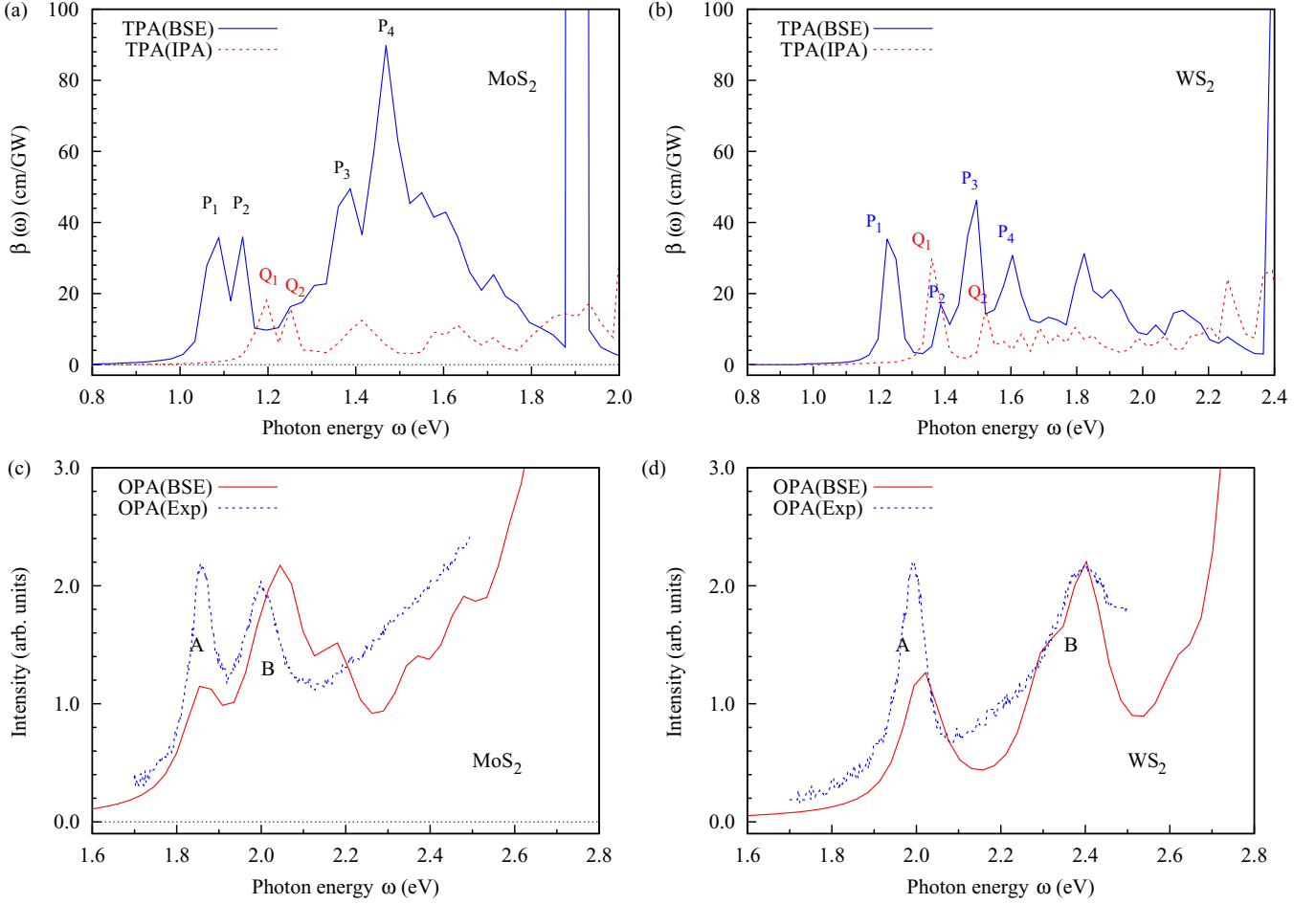
FIG. 3. TPA spectra of (a) MoS_2 and (b) WS_2 monolayers based on the BSE and IPA calculations. Theoretical and experimental [6] OPA spectra of (c) MoS_2 and (d) WS_2 monolayers.

the Q_1 and Q_2 peaks, the P_1 and P_2 peaks have a ∼0.1 eV redshift [Fig. 3(a) and Table II], which suggests a significant excitonic effect. Meanwhile, the energy difference between the P_1 and P_2 peaks is 0.06 eV, which also imply these two peaks could be associated with the spin-orbit coupling effect. To demonstrate this view, we list in Table III the $\sum_k |A^S_{vck}|^2$

(a summation on the k points of the first Brillouin zone) for each $v \rightarrow c$ transition pair used in Eq. (7) for $P_{1,2,3,4}$ peaks of MoS_2 monolayer. As shown in Table III, the transitions at the P_1 and P_2 peaks are dominated by the $v_1 \rightarrow c_2$ and $v_2 \rightarrow c_1$ transition pairs, respectively. Note that in the vicinity of the K point, c_1 and c_2 are almost degenerate. Thus, as

TABLE II. Positions (eV) of OPA and TPA peaks labeled in Fig. 3. E_b is the binding energy of A excitonic state [Figs. 3(c) and 3(d)]. Available experimental and theoretical results are included for comparison.

	OPA			TPA					
	A	E_b	B	P_1	P_2	P_3	P_4	Q_1	Q_2
MoS_2	1.91, 1.78[a], 1.88[b],1.85[c], 1.89[d],1.86[f]	0.25 0.31[f]	2.09, 1.96[a], 2.03[b],1.98[c], 2.03[d],2.00[f]	1.09	1.15	1.38	1.47	1.19	1.25
WS_2	2.10, 1.84[a], 2.00[e],2.02[f]	0.28 0.36[f]	2.52, 2.28[a], 2.39[e], 2.40[f]	1.22	1.36	1.46	1.58	1.36	1.53

[a]GW-BSE calculation [5].

[b]Absorption measurement [42].

[c]PL measurement [43].

[d]Absorption measurement [44].

[e]Absorption measurement [45].

[f]STS measurement [6].
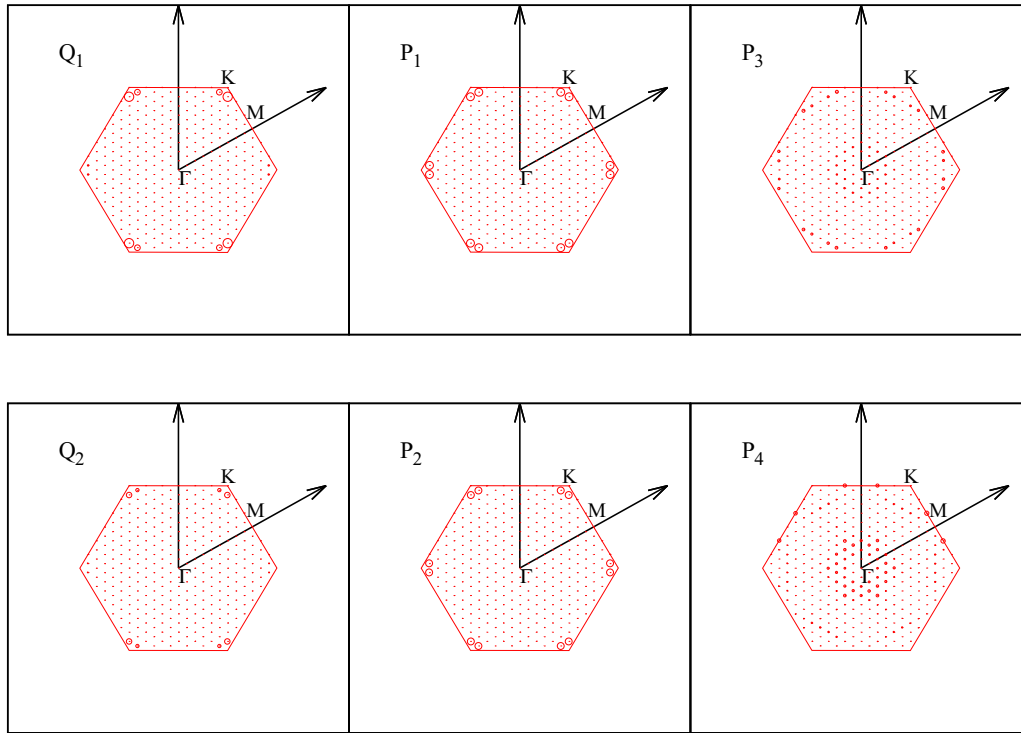
FIG. 4. K points of the first Brillouin zone used in $\sum_{vc}$ [Eq. (5)] and $\sum_{vc}|A^S_{vck}|^2$ [Eq. (7)] for $Q_{1,2}$ and $P_{1,2,3,4}$ peaks of MoS$_2$ monolayer, respectively. The size of point indicates the magnitude of contribution to summation for each k point. The black arrows are the reciprocal vectors.

expected, the spin-orbit coupling leads to the P_1 and P_2 peaks. As for the P_3 and P_4 peaks, the contributions are mainly from the k points around Γ point (Fig. 4), and the corresponding transitions are dominated by the transitions between (v_1, v_2) and (c_1, c_2) (Table III). Similar results can be obtained for WS$_2$ monolayer.

Finally, to obtain an in-depth understanding of electronic transitions in the absorption spectrum, we have checked the projected density of states of MoS$_2$ monolayer. We can see that the valence band edge mainly consist of the d orbital of Mo, which are hybridized with the p orbital of S, and that the

TABLE III. $\sum_k |A^S_{vck}|^2$ for each $v \rightarrow c$ transition pair in summation on the k-points of the first Brillouin zone for $P_{1,2,3,4}$ peaks of MoS$_2$ monolayer. For clarity, eight transition pairs $(23, 24) \rightarrow (27, 28, 29, 30)$ are not shown because their contributions to $\sum_k |A^S_{vck}|^2$ are very small (<0.0001).

v	C	P_1	P_2	P_3	P_4
25 (v_2)	27 (c_1)	0.0[a]	0.9884	0.2136	0.1207
25 (v_2)	28 (c_2)	0.0	0.0	0.2482	0.2180
25 (v_2)	29	0.0	0.0	0.0109	0.0146
25 (v_2)	30	0.0	0.0	0.0338	0.0674
26 (v_1)[b]	27 (c_1)[c]	0.0	0.0	0.3445	0.3003
26 (v_1)[b]	28 (c_2)	0.9994	0.0094	0.1114	0.2083
26 (v_1)[b]	29	0.0	0.0	0.0241	0.0514
26 (v_1)[b]	30	0.0	0.0	0.0125	0.0179

[a]0.0 means the value is small than 0.0001.
[b]The highest valence band (Fig. 1).
[c]The lowest conduction band (Fig. 1).

d orbital of Mo is mainly for the conduction band edge, in agreement with previous reports [9].

C. Comparison between theoretical and experimental results

We make a comparison between theoretical and experimental OPA and TPA spectra for WS$_2$ monolayer. Figure 5 shows two experimental OPA and TPA spectra [18,19] and two theoretical ones for WS$_2$ monolayer. For OPA, as mentioned above, our theoretical A and B excitonic positions with a small rigid shift agree well with other theoretical or experimental results [Figs. 3(c) and 3(d) and Table II]. Overall, Fig. 5(a) shows good agreements between different results. Note that besides the A exciton, the negatively charged trion (labeled by $1s_{tr}$) absorption peak at 2.0 eV was detected in Exp.1 [18] at 10 K. This exciton-trion separation will vanish at the room temperature but detected by applying the electric gating in the two-photon luminescence (TPL) experiments [19]. In particular, there is an excellent agreement between the theoretical (Calc.1) and experimental spectra in terms of peak positions and line shape when a rigid shift of $\sim$0.1 eV is made [see also Fig. 3(d) above]. All three excitonic states (A, B, and C) observed in Exp.2 have been well reproduced by our theoretical calculation.

As for TPA, however, there is no such a good agreement between different results. Due to different applied light ranges and other experimental conditions such as substrate and temperature, only a qualitative comparison to Exp.1 has been made by Zhu *et al.* (Exp.2) [19] based on the two-dimensional hydrogen model. Zhu *et al.* pointed out that the A' and A'' peaks [Fig. 5(b)] of TPA are likely assigned to the excited

FIG. 5. The calculated (Calc.1 [this work] and Calc.2 [17]) and experimental (Exp.1 [18] and Exp.2 [19]) (a) OPA and (b) TPA spectra for WS$_2$ monolayer. (c) The dependence on the scissor value for TPA. (d) Our OPA and TPA spectra are plotted together for ease of comparison. For all TPA spectra, twice input photon energies (2ω) are used to plot. Note that the label 1s and np ($n = 2, 3, 4$) come from the two-dimensional hydrogen model of exciton but deviates substantially from the hydrogen model in energy owing to the novel energy dependence on the orbital angular momentum [18,19].

states of the A exciton. According to the assignment of Exp.1, Zhu *et al.* (Exp.2) have also assigned the A' and A'' peaks [Fig. 5(b)] to 2p(3p) and 3p(4p) states, respectively. We carefully compare environmental factors of these two experiments and prefer to the assignment of 3p and 4p states for Exp.2. Two factors, substrate and temperature, have a potential effect on the band gap of materials [47–49]. As a result, differences in these two factors would change the peak position of optical response of materials [50]. However, Ye *et al.* (Exp.1) have shown that the excitonic energy levels of WS$_2$ monolayer with large binding energy are robust to the changes of both substrate and temperature in their TPL measurements [18]. They suggest that the 2p and 3p excitonic states could be intrinsic for WS$_2$ monolayer, in agreement with those from their *ab initio* GW-BSE calculation in vacuum condition. The energy shift due to these two factors is smaller than 0.1 eV in TPA [18] and OPA [19]. Thus we suggest that the TPLs of two different light source ranges (i.e., 1.0–1.3 in Exp.2 and 1.2–1.5 in Exp.1) should determine three TPA p-type states (i.e., 2p, 3p, and 4p).

We also show in Figs. 5(a) and 5(b) a recent theoretical result (Calc.2) obtained by Berkelbach *et al.* [17] who used a different strategy from ours as explained in Introduction. The Calc.2 has a good agreement with the Exp.1 for the first main

peak of both TPA and OPA. Note that the shifted band gap used in Calc.2 is 2.41 eV which is close to ours (2.38 eV in Table I) but different from one ($\sim$2.7 eV) reported in Exp.1. For OPA, it is well known that the shifted band gap (i.e., scissor correction) only leads to the rigid shift of peak positions [37,51] and does not change the peak intensities. This is not the case for TPA. Here, we show in Fig. 5(c) the scissor value dependence of TPA based on three scissor values (i.e., 0.55, 0.68, and 0.82 eV). We can see that the shifted band gap not only leads to the rigid shift of peak positions (similar to OPA) but also changes the peak intensities. A change in peak intensities can be understood in terms of Eq. (9) in which the denominator ($E_m^S - \hbar\omega$) includes the scissor correction. Thus the differences in peak positions are likely due to the differences in the band gap. However, at present, we cannot completely rationalize this relationship because the band gaps are very different from different experimental and theoretical results for MoS$_2$ and WS$_2$ monolayers [4,5,9,24,31,41] (see also Table I). For example, the band gaps of MoS$_2$ monolayer based on different methods range from 2.15 to 2.97 eV.

In our theoretical TPA spectrum, if we assign the P$_1$ peak to the excited state of the A exciton, the P$_2$ peak could be assigned to the excited state of the B exciton because the P$_1$ and P$_2$ peaks are associated with the spin-orbit splitting

at similar k points to the A and B excitonic peaks (see Fig. 4 and Ref. [2].). We assign the excitonic state of the P1 peak to the $3p$ state in the two-dimensional hydrogen model for two reasons. One is our calculated OPA spectrum is in good agreement with the experimental results in terms of peak positions with a small shift, which means the positions of excited states (both light and dark states) should be reliable. The other is that in two experimental measurements (Exp.1 and Exp.2) the $3p$ state locates near the B excitonic state, which also occurs in our theoretical results [Fig. 5(d)]. Similarly, according to the position of C peak in OPA, we suggest that the peaks above 2.7 eV in Exp.2 should be matched with those in our theoretical spectrum. Finally, for 2.7 eV $< 2\omega <$ 3.2 eV in Fig. 5(d), the *alternative* peaks in OPA and TPA spectra indicate the ability of TPA in probing the excitonic dark states. Overall, our theoretical TPA spectra are partially consistent with two experimental ones, and no occurrence of the $2p$ state in our results opens up a question which cannot be answered at present.

IV. CONCLUSIONS

We have presented a first-principles many-body formalism based on the BSE eigenstates for calculating the TPA spectrum of two-dimensional semiconductor materials. As applications, we have used this formalism to calculate the TPA spectra of MoS_2 and WS_2 monolayers. Compared to the IPA-TPA spectra, the BSE-TPA ones exhibit significant excitonic effects. By tracing the SOS process, we find that the first two BSE-TPA peaks on the onset of spectrum mainly originate from the transitions between the valance and conduction band edges at the vicinity of K point. At the higher applied photon energy, the two BSE-TPA peaks are dominated by the transitions at the k points around Γ point. For WS_2 monolayer, the calculated BSE-TPA spectrum is partially consistent with the experimental ones in terms of peak positions and line shape, and thus a further study is necessary. Our theoretical BSE-TPA spectrum of MoS_2 will be an important reference for experiments due to the similarity of electronic structures of MoS_2 and WS_2 monolayer.

[1] M. del CastilloMussot and L. J. Sham, Phys. Rev. B **31**, 2092 (1985).

[2] R. Gillen and J. Maultzsch, IEEE J. Sel. Top. Quantum Electron. **23**, 219 (2017).

[3] G. P. P. Giuseppe Grosso, *Solid State Physics*, 2nd ed. (Elsevier, Singapore, 2013).

[4] A. Molina-Sánchez, D. Sangalli, K. Hummer, A. Marini, and L. Wirtz, Phys. Rev. B **88**, 045412 (2013).

[5] A. Ramasubramaniam, Phys. Rev. B **86**, 115409 (2012).

[6] A. F. Rigosi, H. M. Hill, K. T. Rim, G. W. Flynn, and T. F. Heinz, Phys. Rev. B **94**, 075440 (2016).

[7] M. Rohlfing and S. G. Louie, Phys. Rev. B **62**, 4927 (2000).

[8] M. Rohlfing and S. G. Louie, Phys. Rev. Lett. **81**, 2312 (1998).

[9] H. Shi, H. Pan, Y.-W. Zhang, and B. I. Yakobson, Phys. Rev. B **87**, 155304 (2013).

[10] R. Leitsmann, W. G. Schmidt, P. H. Hahn, and F. Bechstedt, Phys. Rev. B **71**, 195209 (2005).

[11] A. Taghizadeh and T. G. Pedersen, Phys. Rev. B **99**, 235433 (2019).

[12] A. Taghizadeh and T. G. Pedersen, Phys. Rev. B **97**, 205432 (2018).

[13] C. Attaccalite, E. Cannuccia, and M. Grüning, Phys. Rev. B **95**, 125403 (2017).

[14] E. K. Chang, E. L. Shirley, and Z. H. Levine, Phys. Rev. B **65**, 035205 (2001).

[15] G. Wang, X. Marie, I. Gerber, T. Amand, D. Lagarde, L. Bouet, M. Vidal, A. Balocchi, and B. Urbaszek, Phys. Rev. Lett. **114**, 097403 (2015).

[16] C. Attaccalite, M. Grüning, H. Amara, S. Latil, and F. mboxçelse çfiois Ducastelle, Phys. Rev. B **98**, 165126 (2018).

[17] T. C. Berkelbach, M. S. Hybertsen, and D. R. Reichman, Phys. Rev. B **92**, 085413 (2015).

[18] Z. Ye, T. Cao, K. O'Brien, H. Zhu, X. Yin, Y. Wang, S. G. Louie, and X. Zhang, Nature (London) **513**, 214 (2014).

[19] B. Zhu, X. Chen, and X. Cui, Sci. Rep. **5**, 9218 (2015).

[20] S. Chen, M.-L. Zheng, X.-Z. Dong, Z.-S. Zhao, and X.-M. Duan, J. Opt. Soc. Am. B **30**, 3117 (2013).

[21] V. Nathan, A. H. Guenther, and S. S. Mitra, J. Opt. Soc. Am. B **2**, 294 (1985).

[22] J. P. Perdew, K. Burke, and M. Ernzerhof, Phys. Rev. Lett. **78**, 1396 (1997).

[23] Y. Mokrousov, G. Bihlmayer, and S. Blügel, Phys. Rev. B **72**, 045402 (2005).

[24] D. Y. Qiu, F. H. da Jornada, and S. G. Louie, Phys. Rev. Lett. **111**, 216805 (2013).

[25] W. Song and L. Yang, Phys. Rev. B **96**, 235441 (2017).

[26] M. Rohlfing and J. Pollmann, Phys. Rev. B **63**, 125201 (2001).

[27] A. Szabo and N. S. Ostlund, *Modern Quantum Chemistry Intro Advanced Electronic Structure Theory* (Dover Publications, INC. Mineola, New York, 1996).

[28] R. Del Sole and R. Girlanda, Phys. Rev. B **48**, 11789 (1993).

[29] J. E. Sipe and E. Ghahramani, Phys. Rev. B **48**, 11705 (1993).

[30] K. Dewhurst, S. Sharma, L. Nordström, F. Cricchio, F. Bultmark, O. Gräs, and H. Gross, see http://elk.sourceforge.net.

[31] T. Cheiwchanchamnangij and W. R. L. Lambrecht, Phys. Rev. B **85**, 205302 (2012).

[32] E. S. Kadantsev and P. Hawrylak, Solid State Commun **152**, 909 (2012).

[33] V. Shahnazaryan, I. Iorsh, I. A. Shelykh, and O. Kyriienko, Phys. Rev. B **96**, 115409 (2017).

[34] H. M. Hill, A. F. Rigosi, K. T. Rim, G. W. Flynn, and T. F. Heinz, Nano Lett. **16**, 4831 (2016).

[35] C. Zhang, A. Johnson, C.-L. Hsu, L.-J. Li, and C.-K. Shih, Nano Lett. **14**, 2443 (2014).

[36] C. Kastl, C. T. Chen, R. J. Koch, B. Schuler, T. R. Kuykendall, A. Bostwick, C. Jozwiak, T. Seyller, E. Rotenberg, A. Weber-Bargioni, S. Aloni, and A. M. Schwartzberg, 2D Mater. **5**, 045010 (2018).

[37] S. Z. Karazhanov, P. Ravindran, A. Kjekshus, H. Fjellvåg, and B. G. Svensson, Phys. Rev. B **75**, 155104 (2007).

[38] G. Onida, L. Reining, and A. Rubio, Rev. Mod. Phys. **74**, 601 (2002).

[39] H. M. Hill, A. F. Rigosi, C. Roquelet, A. Chernikov, T. C. Berkelbach, D. R. Reichman, M. S. Hybertsen, L. E. Brus, and T. F. Heinz, Nano Lett. **15**, 2992 (2015).

[40] A. R. Klots, A. K. M. Newaz, B. Wang, D. Prasai, H. Krzyzanowska, J. Lin, D. Caudel, N. J. Ghimire, J. Yan, B. L. Ivanov, K. A. Velizhanin, A. Burger, D. G. Mandrus, N. H. Tolk, S. T. Pantelides, and K. I. Bolotin, Sci. Rep. **4**, 6608 (2014).

[41] H.-P. Komsa and A. V. Krasheninnikov, Phys. Rev. B **86**, 241201(R) (2012).

[42] K. F. Mak, C. Lee, J. Hone, J. Shan, and T. F. Heinz, Phys. Rev. Lett. **105**, 136805 (2010).

[43] A. Splendiani, L. Sun, Y. Zhang, T. Li, J. Kim, C.-Y. Chim, G. Galli, and F. Wang, Nano Lett. **10**, 1271 (2010).

[44] Y. V. Morozov and M. Kuno, Appl. Phys. Lett. **107**, 083103 (2015).

[45] Y. Li, A. Chernikov, X. Zhang, A. Rigosi, H. M. Hill, A. M. van der Zande, D. A. Chenet, E.-M. Shih, J. Hone, and T. F. Heinz, Phys. Rev. B **90**, 205422 (2014).

[46] E. B. Barros, R. B. Capaz, A. Jorio, G. G. Samsonidze, A. G. Souza Filho, S. Ismail-Beigi, C. D. Spataru, S. G. Louie, G. Dresselhaus, and M. S. Dresselhaus, Phys. Rev. B **73**, 241406(R) (2006).

[47] X. Z. Du, J. Li, J. Y. Lin, and H. X. Jiang, Appl. Phys. Lett. **111**, 132106 (2017).

[48] A. Franceschetti, Phys. Rev. B **76**, 161301(R) (2007).

[49] B. Pejova, B. Abay, and I. Bineva, J. Phys. Chem. C **114**, 15280 (2010).

[50] J. Petalas, S. Logothetidis, M. Gioti, and C. Janowitz, Physica Status Solidi (b) **209**, 499 (1998).

[51] E. Luppi, H. Hübener, and V. Véniard, Phys. Rev. B **82**, 235201 (2010).